JMEPEG (2020) 29:6591–6604
https://doi.org/10.1007/s11665-020-05132-x

1059-9495/$19.00

Physical Model Based on Data-Driven Analysis of Chemical Composition Effects of Friction Stir Welding

J.Y. Li, X.X. Yao, and Z. Zhang

(Submitted May 28, 2020; in revised form July 24, 2020; published online September 23, 2020)

Variations in chemical compositions can lead to changes in the mechanical properties during friction stir welding (FSW). To facilitate control over the final mechanical properties of the friction stir weld, the relationship between the chemical compositions and final mechanical properties must be investigated. An artificial neural network was used for a data-driven analysis of the effects that chemical compositions have on the mechanical properties of FSW. A precipitate evolution model was implemented to examine the detailed contributions of different elements to the final mechanical properties. Experiments with different chemical compositions were conducted to validate the established models. Through both numerical and experimental analyses, it was determined that the yield strength in the stir zone increased with an increase in Mg/Si owing to the formation of Mg_2Si. The mechanical properties also increased with Si, Mg, and Cu contents in the solid solution. The mechanical properties decreased with an increase in the Fe and Mn contents owing to the formation of an intermetallic compound α-$Al_x(MnFe)_ySi_z$. The final mechanical properties were determined by both the welding temperature and chemical compositions. By utilizing a physical model based on a data-driven analysis, the mechanical properties could be optimally controlled.

Keywords aluminum alloy, chemical composition, friction stir welding, mechanical property

1. Introduction

The final quality of a friction stir weld is controlled by many factors, including the rotational speed, transverse speed, penetration depth, tool geometry, and tilt angle (Ref 1-7). A higher rotational speed or lower transverse speed in friction stir welding (FSW) can lead to an increase in the welding temperature (Ref 8-10). An increase in the welding temperature can lead to a higher solution of precipitates for aluminum alloys during the heating process (Ref 11). During the cooling process, the precipitates can nucleate and grow. A higher volume fraction of precipitates with small average particle sizes (in nanoscale) can lead to an increase in the hardness, as well as the yield strength, of the final friction stir welds (Ref 12, 13). Although the design of welding parameters can optimize the weld quality in FSW, experimental tests reveal that the mechanical properties of friction stir welds can vary even under the same (or similar) welding parameters. Abdulstaar et al. (Ref 14) found that when the rotational and transverse speeds are 1200 rpm and 0.8 mm/s, respectively, the hardness is approximately 60 HV in the stir zone during the FSW of AA6061. When the rotational and transverse speeds are 1200 rpm and 0.7 mm/s, respectively, Fadaeifard et al. (Ref 15) found that the average hardness in the nugget zone is 59.85 HV. Liu and Ma (Ref 16) demonstrated the effect of rotational speed on the hardness in the stir zone during the FSW of AA6061. When the rotational speed is 1200 rpm and the transverse speed is 3.3 mm/s, the hardness in the stir zone ranges from 59.6 to 76.6 HV. However, when the rotational and transverse speeds are decreased to 1000 rpm and 1.7 mm/s, respectively, the hardness in the stir zone during the FSW of AA6061 is only 47 HV in the as-weld state (Ref 11). For AA6063, the hardness in the stir zone ranges from 40 to 45 HV when the rotational speed is changed from 800 to 1220 rpm (Ref 17). As evidenced, the hardness in the stir zone during FSW can vary depending upon the welding conditions. Even under the same or similar welding conditions, the hardness of the welded material can vary because of changes in the chemical compositions. It is essential to investigate how chemical compositions affect the final mechanical properties of elements that undergo FSW. The determination of these internal relationships relies on statistical and theoretical analyses.

An artificial neural network (ANN) is an efficient tool to analyze the effects of the chemical compositions during FSW. Through a data-driven analysis, the correlation between the chemical compositions and final mechanical properties can be established. This method has been successfully applied to processing techniques. Wang et al. (Ref 18, 19) constructed multilevel data-driven surrogate models based on extensive computational data with limited experimental data to predict microstructural evolutions in additive manufacturing. Big data-based analytics were used by Majeed et al. (Ref 20) to optimize the production performance in additive manufacturing. Yan et al. (Ref 21) optimized numerous influential factors to present a comprehensive material model of the process–structure–property relationships present in additive manufacturing.

Although many beneficial studies focus on a data-driven analysis in various manufacturing industries, the combination of a data-driven analysis with FSW is lacking. The problem lies in the combination of a physical model with a data-driven

J.Y. Li, X.X. Yao, and **Z. Zhang**, State Key Laboratory of Structural Analysis for Industrial Equipment, Department of Engineering Mechanics, Faculty of Vehicle Engineering and Mechanics, Dalian University of Technology, Dalian 116024, China. Contact e-mail: zhangz@dlut.edu.cn.

analysis, which must be resolved to apply this method to FSW. The internal relationships between the input welding parameters and the output welding quality are already established through many useful methods. The Monte Carlo model allows the welding parameters to be linked to the recrystallized grain morphologies (Ref 22-24). A precipitate evolution model (PEM) allows the welding parameters to be linked with the final mechanical properties, including the hardness and yield strength (Ref 11, 25, 26). For defect-free FSW, it is necessary to establish the direct relationship between the input variables and the final mechanical properties, especially the effects of various chemical compositions on the mechanical properties, which should be studied in detail. Doing so will allow various manufacturing industries to facilitate control over the final quality of FSW.

2. Experimental Procedure

Three specimens of 6xxx aluminum alloys with different chemical compositions were friction stir welded using an FSW machine. Electron-dispersive spectroscopy (EDS) was used to measure the chemical compositions of the specimens. The chemical compositions are summarized in Table 1. The dimensions of the specimens were 200 × 110 × 4 mm. H13 steel was used, and it had a shoulder diameter of 12 mm and a conical pin. The diameter of the pin ranged from 3 mm at the tip to 4 mm at the top. The length of the pin was 3.8 mm, which was slightly shorter than the weld thickness to ensure defect-free welding. The rotational speed was 800 rpm, and the transverse speed was 200 mm/min. An infrared radiation thermometer (IRT) system was used to measure the welding temperatures. A Vickers hardness tester was used to measure the hardness distributions of different chemical compositions in the friction stir weld. The equipment used for experiment is shown in Fig. 1.

3. Model Descriptions

3.1 Moving Heat Source Model

At present, many numerical models can be used to simulate FSW, e.g., fully coupled thermomechanical model (Ref 9), adaptive re-meshing model (Ref 27, 28), CFD model (Ref 29, 30), and moving heat source model (Ref 31-33). The moving heat source model was established with the ABAQUS subroutine DFLUX to simulate the heat generated by friction between the welding tool and the specimen. Both the introduction and application of the moving heat source model have been discussed in detail in previous studies (Ref 31-33). To calculate the input power of the moving heat source model, we used the following formula (Ref 34):

$$P_s = \eta \frac{2}{3} \pi \mu p \omega \left(r_s^3 + 3 l_p r_p^2 \right), \quad \text{(Eq 1)}$$

where η is the frictional heat ratio flowing into the welded components and was taken at 0.39, μ is the friction coefficient (0.5), p is the contact pressure that was lower than the actual flow stress of the material at the working temperature (Ref 35), ω is the rotational speed of the welding tool, r_s is the radius of the shoulder, r_p is the radius of the pin at the top, and l_p is the length of the pin. The values of ω, r_s, r_p, and l_p were identical to the experimental settings. The boundary conditions for the convective heat transfer were as follows:

$$k \frac{\partial T}{\partial n} = h(T - T_a), \quad \text{(Eq 2)}$$

where k is the thermal conductivity and h is the convective heat transfer coefficient, as stated in the literature (Ref 36). T_a is the ambient temperature (20 °C). Using the moving heat source model, the temperature history of each point (mesh point) on the specimen was calculated under various conditions.

3.2 PEM

During FSW, the microstructure changed with a variation in temperature, leading to a change in the mechanical properties. The strengthening mechanism of the Al alloys originated from four items, which were grain size, dislocation density, precipitates, and a solid solution. The direct contribution from grain size was insignificant in comparison with those of the other three items (Ref 26). The precipitates provided the main contribution to the calculation of the yield stress (Ref 11). The PEM included the nucleation, dissolution, and coarsening of the precipitates. The nucleation rate was expressed as follows (Ref 11):

$$j = j_0 \exp\left[-\left(\frac{A_0}{RT} \right)^3 \left(\frac{1}{\ln(\bar{C}/C_e)} \right)^2 \right] \exp\left(-\frac{Q_d}{RT} \right), \quad \text{(Eq 3)}$$

Table 1 Chemical compositions of specimens (wt.%)

Specimen	Mg	Si	Cu	Fe	Mn	Al
No. 1	0.85	0.64	0.26	0.54	0.00	97.42
No. 2	0.88	0.61	0.23	0.17	0.04	97.93
No. 3	0.82	0.82	0.51	0.71	0.15	96.8

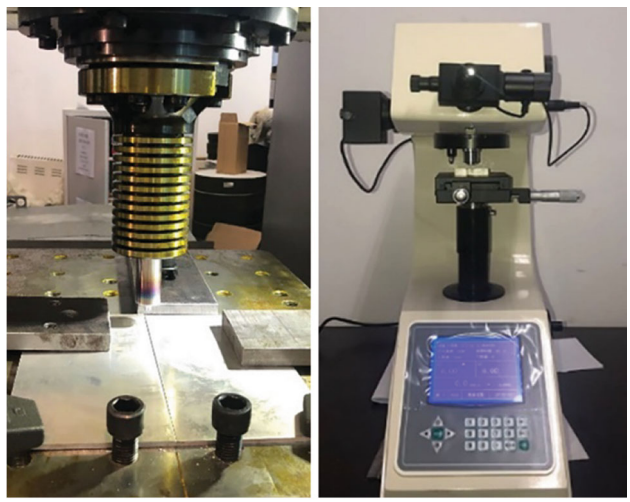

(a) (b)

Fig. 1 Friction stir welding (FSW) machine and Vickers hardness tester. (a) Friction stir welding machine, (b) Vickers hardness tester

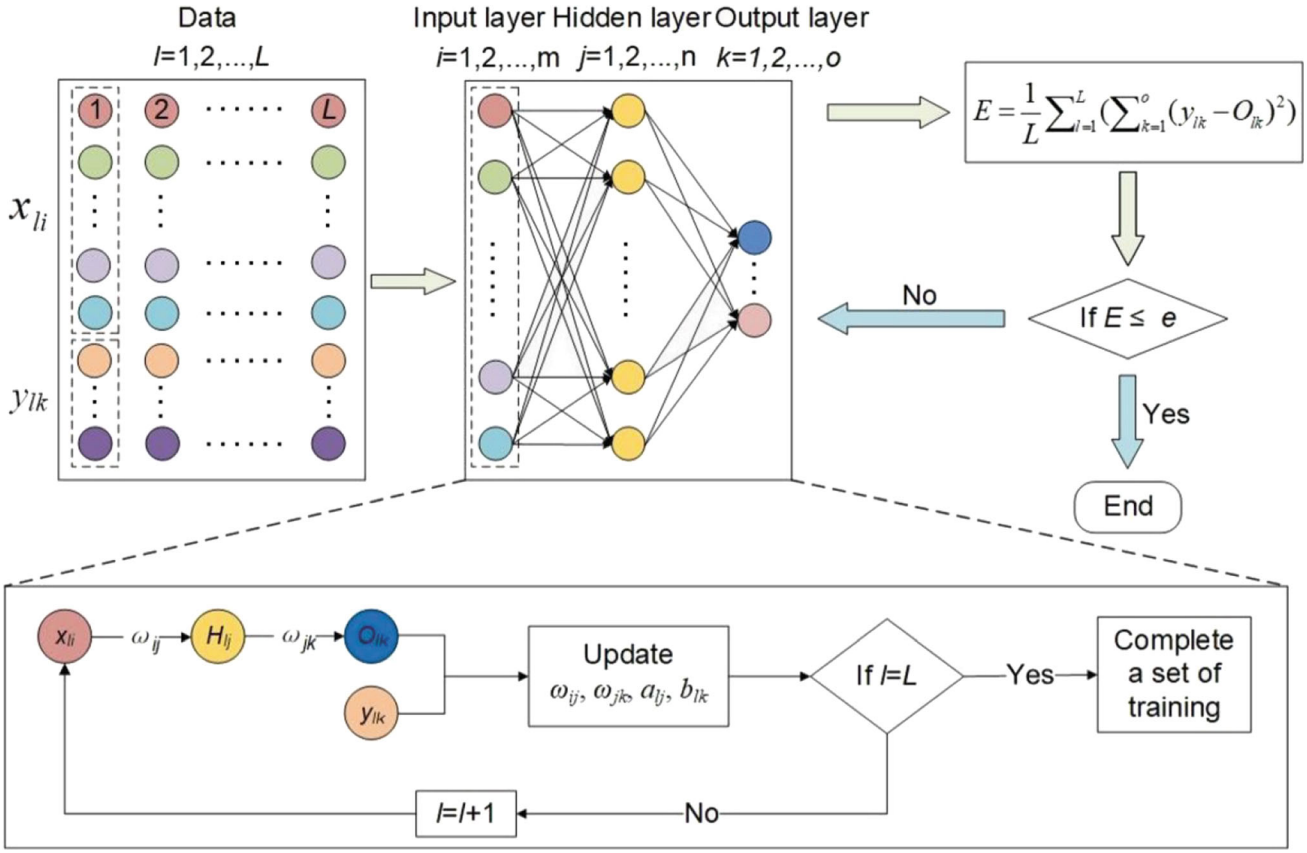

Fig. 2 Back-propagation (BP) artificial neural network (ANN) model workflow

where j_0 is a pre-exponential term and was taken at 9.66×10^{34} s/m^3. A_0 is a parameter related to the energy barrier for nucleation (16.22 kJ/mol). R (8.314 J/K/mol) is the universal gas constant, T is the temperature, $\bar{C}$ is the mean solute content in the matrix, and C_e is the equilibrium solute content at the particle/matrix interface. Q_d is the activation energy for diffusion and was taken at 130 kJ/mol. The rate of growth, or dissolution of the precipitates, was calculated as follows:

$$v = \frac{\bar{C} - C_i}{C_p - C_i}\frac{D}{r}, \quad \text{(Eq 4)}$$

where C_i is the solute concentration at the particle/matrix interface, C_p is the concentration of the element within the particle and was taken at 63.4 wt.%, D is the diffusion coefficient, and r is the particle radius. The relationship between C_i and C_e was the following:

$$C_i = C_e \exp\left(\frac{2\gamma V_m}{rRT}\right), \quad \text{(Eq 5)}$$

where γ is the particle/matrix interfacial energy (0.2) and V_m is the molar volume of the precipitates (3.95×10^{-5} m^3/mol).

The contribution to the yield strength from the hardening precipitates was calculated as follows:

$$\sigma_P = \frac{M}{b\bar{r}}\left(2\beta G b^2\right)^{-1/2}\left(\frac{3f}{2\pi}\right)^{1/2}\left(\frac{\sum_i N_i F_i}{\sum_i N_i}\right)^{3/2}, \quad \text{(Eq 6)}$$

where M is the Taylor factor (3.1), b is the magnitude of the Burgers vector (2.84×10^{-10}), and $\bar{r}$ is the mean particle radius. β is a constant representing the dislocation line tension and was taken at 0.36. G is the shear modulus of the aluminum matrix (2.7×10^{10} N/m^3), f is the volume fraction, and N_i is the number density of particles that belonged to a given size class (r_i). F_i is the function of the particle radius r_i. When r_i was smaller than the critical radius r_c,

$$F_i = 2\beta G b^2\left(\frac{r_i}{r_c}\right). \quad \text{(Eq 7)}$$

When r_i was larger than the critical radius r_c,

$$F_i = 2\beta G b^2. \quad \text{(Eq 8)}$$

Some of the Mg, Si, and Cu elements existed in the solid solution as solutes. Therefore, the contribution from the solid solution to the yield strength was expressed as follows:

$$\sigma_{ss} = k_{Mg} C_{Mg}^{2/3} + k_{Si} C_{Si}^{2/3} + k_{Cu} C_{Cu}^{2/3}, \quad \text{(Eq 9)}$$

where C_{Mg}, C_{Si}, and C_{Cu} are the concentrations of Mg, Si, and Cu, respectively, in the solid solution. The corresponding scaling factors are k_{Mg}, k_{Si}, and k_{Cu} and were taken at 66.3, 29, and 46.4 MPa/wt.%$^{2/3}$, respectively.

In the 6xxx series aluminum alloys, a portion of the Si elements can be combined with Fe and Mn to form α-$Al_x(MnFe)_ySi_z$ (Ref 37, 38). The formation of this intermetallic compound is frequently affected by the processing technology and chemical composition of the matrix. Unlike Mg_2Si, the

Table 2 Data for training ANN model of peak welding temperature

Rotational speed, rpm	Welding speed, mm/min	Thickness, mm	Shoulder diameter, mm	Peak temperature, °C	Ref.
390	141.8	8.13	25.4	475	42
500	140	6	24	471	43
300	120	6.4	9.6	425	44
400	120	6.4	9.6	433	44
650	120	6.4	9.6	454	44
1000	120	6.4	9.6	472	44
1200	200	3	10	511.8	45
1500	118	5	15	496	46
900	200	6	24	439	47
1200	200	6	24	467	47
1400	200	6	24	482	47
1400	400	6	24	477	47
1400	600	6	24	472	47
800	30	8	24	481	48
1400	800	5	16	462.7	49
1200	600	5	16	435	50
1200	800	5	16	420	50
573	60	10	12.5	456	50

larger size of α-$Al_x(MnFe)_ySi_z$ indicates it cannot directly contribute to the calculation of the yield strength. Myhr et al. calculated the effect of this compound on the mechanical properties in the form of α-$Al_{15}(MnFe)_3Si_3$ (Ref 39). However, other experiments (Ref 40) show that the yield strength is reduced when the Fe content is increased. This phenomenon is supported by the concept of effective Si content in the solid solution (Ref 39):

$$C_{\mathrm{Si}}^{\mathrm{eff}} = C_{\mathrm{Si}} - 0.33 * (C_{\mathrm{Fe}} + C_{\mathrm{Mn}}), \quad \text{(Eq 10)}$$

where C_{Fe} and C_{Mn} are the concentrations of Fe and Mn, respectively, in the solid solution.

The yield strength was expressed as follows:

$$\sigma_{\mathrm{y}} = \sigma_0 + \sigma_{\mathrm{ss}} + \sigma_{\mathrm{p}}, \quad \text{(Eq 11)}$$

where the contribution from the grain size of pure Al to the yield strength (σ_0) is taken as 10 MPa (Ref 25, 26).

3.3 ANN Model

Data-driven methods can be applied to process mechanics for the prediction of product quality in engineering (Ref 18, 19, 41). The classic response surface method, Gaussian process model, and ANN are generally used in a data-driven design. In this study, a three-layer back-propagation (BP) ANN was employed to build the surrogate model. A traditional three-layer BP ANN is composed of an input layer, a hidden layer, and an output layer, as shown in Fig. 2. x_{li} is the data related to the input parameters, while y_l is the data related to the output parameters. L is the number of data groups, m is the number of input parameters, n is the number of hidden layers, and k is the number of output parameters. The input data from the input layer are summed with the weight (ω_{ij}) between the input layer and the hidden layer. The calculated results of each neuron in the hidden layer are shown as follows:

$$H_{lj} = g\left(\sum_{i}^{m} x_{li}\omega_{ij} + a_{lj}\right), \quad \text{(Eq 12)}$$

where g is the activation function and a_{lj} is the threshold value. Similarly, H_{lj} on the neurons in the hidden layer was further transmitted to the output layer, and the calculation results (O_{lk}) were then obtained through the output layer as follows:

$$O_{lk} = g\left(\sum_{j}^{n} H_{lj}\omega_{jk} + b_{lk}\right), \quad \text{(Eq 13)}$$

where ω_{jk} is the weight between the hidden layer and the output layer and b_{lk} is the threshold value.

The data training was completed by updating the connection weight between each layer. Only the adjacent neurons in the two layers were influenced by one another. The weight updating formula used was the following:

$$\begin{cases} \omega_{ij(\mathrm{new})} = \omega_{ij(\mathrm{old})} + \eta\dfrac{\partial E}{\partial \omega_{ij(\mathrm{old})}}\omega_{ij(\mathrm{old})} \\ \omega_{jk(\mathrm{new})} = \omega_{jk(\mathrm{old})} + \eta\dfrac{\partial E}{\partial \omega_{jk(\mathrm{old})}}\omega_{jk(\mathrm{old})} \end{cases}, \quad \text{(Eq 14)}$$

where η is the learning efficiency. The update to the threshold was the following:

$$\begin{cases} a_{lj(\mathrm{new})} = a_{lj(\mathrm{old})} + \eta\dfrac{\partial E}{\partial a_{lj(\mathrm{old})}}a_{ij(\mathrm{old})} \\ b_{lk(\mathrm{new})} = b_{lk(\mathrm{old})} + \eta\dfrac{\partial E}{\partial b_{lk(\mathrm{old})}}b_{lk(\mathrm{old})} \end{cases}. \quad \text{(Eq 15)}$$

After updating the weights and thresholds, the above process was repeated with a new dataset until all the data had been trained. We calculated the performance indicators to determine the end of the training:

$$E = \frac{1}{L}\sum_{l=1}^{L}\left(\frac{1}{2}\right)\sum_{k=1}^{O}(y_{lk} - O_{lk})^2 \quad \text{(Eq 16)}$$

If E was less than or equal to the accuracy, the training was completed. Otherwise, we retrained with updated thresholds and weights until accuracy was met.

Table 3 Input data for training ANN model of mechanical properties

No.	Mg, wt.%	Si, wt.%	Cu, wt.%	Mn, wt.%	Fe, wt.%	Peak temperature, °C	Ref.
1.	0.9400	0.5300	0.2000	0.0061	0.4000	447.9356	51
2.	0.9400	0.5000	0.2000	0.0060	0.4000	482.6922	52
3.	0.9200	0.6500	0.2900	0.7000	0.3200	446.8285	53
4.	0.9910	0.5740	0.1990	0.0380	0.3500	426.4920	54
5.	1.0300	0.7400	0.3100	0.0800	0.1900	455.9699	55
6.	0.9200	0.5700	0.2100	0.0300	0.1700	491.5189	56
7.	0.8400	0.5400	0.2400	0.0100	0.4000	481.9583	57
8.	1.0000	0.7000	0.4000	0.1000	0.7000	563.3883	58
9.	1.0700	0.5800	0.2400	0.1000	0.3200	427.8641	59
10.	0.9900	0.5900	0.2300	0.0090	0.1200	501.8456	60
11.	0.9600	0.5800	0.2800	0.0300	0.4100	467.6291	61
12.	0.6900	0.9100	0.0620	0.5600	0.2300	481.9583	57
13.	0.7000	1.3000	0.1200	0.7000	0.5100	496.0129	62
14.	0.9200	1.3100	0.0430	0.5800	0.2400	406.2821	63
15.	0.7800	0.9500	0.0800	0.4800	0.3900	570.9107	64
16.	0.5900	0.9600	0.0100	0.4500	0.1900	499.4842	65
17.	0.8000	1.0500	0.0400	0.6800	0.2600	505.7730	66
18.	1.1800	0.8900	0.3100	0.4000	0.4000	444.3964	67
19.	0.7000	1.0000	0.0700	0.5100	0.0800	469.4877	68
20.	1.1100	1.2100	0.0958	0.4850	0.3780	423.5751	Calculated by PEM
21.	0.9300	1.1300	0.0965	0.6530	0.2270	423.5751	
22.	1.0300	1.0100	0.0166	0.9490	0.4800	423.5751	
23.	0.9000	0.8400	0.0971	0.8750	0.1140	423.5751	
24.	0.6300	1.1800	0.0958	0.9760	0.2760	423.5751	
25.	0.7800	1.1800	0.0491	0.4930	0.2530	423.5751	
26.	0.7600	0.8000	0.0802	0.4210	0.4060	423.5751	
27.	0.6000	0.8200	0.0747	0.5980	0.1690	423.5751	
28.	0.8600	0.7500	0.3490	0.0990	0.2373	423.5751	
29.	0.8500	0.6400	0.1970	0.0250	0.3294	423.5751	
30.	0.8900	0.4500	0.2720	0.0190	0.1599	423.5751	
31.	1.0200	0.4900	0.2610	0.0750	0.3471	423.5751	
32.	1.1600	0.4400	0.3120	0.1440	0.1111	423.5751	
33.	1.1300	0.7300	0.3270	0.0520	0.1969	423.5751	
34.	0.8300	0.4530	0.2123	0.0989	0.2779	423.5751	
35.	0.9700	0.4300	0.1653	0.0103	0.1268	423.5751	
36.	1.0600	0.4400	0.2908	0.1388	0.3801	423.5751	
37.	1.0900	0.5100	0.1553	0.0059	0.0138	423.5751	
38.	1.1500	0.5700	0.2162	0.1486	0.1755	423.5751	

To avoid data singularity, the input data of the neural network needed to be normalized:

$$x' = \frac{x - x_{\min}}{x_{\max} - x_{\min}}, \quad \text{(Eq 17)}$$

where x is the original data and $x_{\max}$ and $x_{\min}$ are the maximum and minimum values of the data, respectively. Similarly, the output of the trained neural network needed to be normalized:

$$l' = \frac{l - l_{\min}}{l_{\max} - l_{\min}}, \quad \text{(Eq 18)}$$

where l' is the normalized output value and $l_{\max}$ and $l_{\min}$ are the maximum and minimum values of the original output data.

The Levenberg–Marquardt algorithm was used for the training in Eq 12. During the training process, the log-sigmoid function was used for the activation functions between layers. The log-sigmoid function formula is as follows:

$$g(x) = \frac{1}{1 + e^{-x}}. \quad \text{(Eq 19)}$$

4. Physical Model Based on Data-Driven Analysis and Experimental Validation

The combination of a physical model with a data-driven analysis was a key component of this study. The data came from both the PEM and the FSW experiment. Because the variations in the mechanical properties were directly related to the PEM, the mechanical changes under different conditions could be explained in theory. A comparison of the experimental and numerical results could validate the proposed physical model based on a data-driven analysis. Because the welding temperature determines the microstructural evolutions, both the peak temperature and mechanical property were predicted by the physical model based on the data-driven analysis. The weight and thresholds in the ANN model of the peak welding temperature were trained by experimental data from the literature (Ref 42-50), as shown in Table 2. The weight and threshold values in the ANN model of the mechanical property were trained by both experimental data and the PEM results, as shown in Tables 3 and 4.

Table 4 Output data for training ANN model of mechanical properties

Number	Centerline, HV	*D*/4, HV	*D*/2, HV	Ref.
1.	80.90	73.08	82.87	51
2.	80.34	82.24	65.59	52
3.	56.32	58.04	70.55	53
4.	66.28	69.64	54.65	54
5.	89.26	97.94	105.59	55
6.	74.75	75.33	65.33	56
7.	79.48	73.94	83.82	57
8.	62.59	60.84	70.45	58
9.	69.01	70.38	72.82	59
10.	77.76	83.48	70.45	60
11.	76.52	79.32	76.71	61
12.	77.38	83.67	73.19	57
13.	76.57	76.05	73.99	62
14.	72.06	74.12	87.53	63
15.	84.02	78.34	85.44	64
16.	71.82	73.79	84.85	65
17.	77.98	84.85	85.58	66
18.	83.04	83.53	77.06	67
19.	83.76	79.79	74.23	68
20.	83.94	85.80	99.86	Calculated by PEM
21.	78.07	79.44	90.64	
22.	68.41	69.76	80.74	
23.	68.60	69.72	83.17	
24.	70.69	72.32	88.78	
25.	74.58	76.64	96.86	
26.	68.27	70.03	88.27	
27.	65.20	66.77	82.48	
28.	74.97	75.87	92.53	
29.	68.85	69.64	87.55	
30.	66.76	68.42	85.59	
31.	63.50	65.04	80.65	
32.	64.70	66.27	82.13	
33.	81.08	82.94	97.03	
34.	60.87	62.36	76.99	
35.	64.44	66.08	82.95	
36.	56.00	57.24	69.26	
37.	68.70	69.67	84.91	
38.	64.41	66.40	88.69	

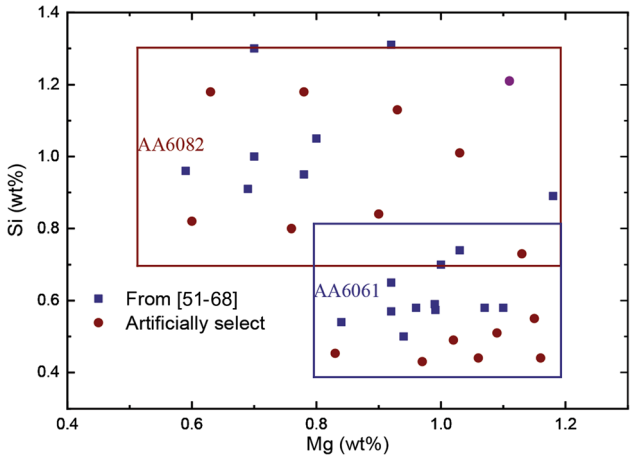

Fig. 3 Mg and Si contents in 6xxx series Al alloys

The contents of the Mg and Si in the 6xxx series Al alloys are shown in Fig. 3. Under the same welding conditions, the Mg, Si, and other elements could be different for the same materials. This was the primary reason that the final mechanical property could be different even after FSW for the same material under the same welding conditions. Therefore, the effects of the chemical compositions on the final mechanical properties must be clarified.

The peak temperature measured by the IRT system is 430.3 °C, as shown in Fig. 4(a). The peak temperature predicted by the ANN model is 423.6 °C, and the calculated peak temperature by finite element model (FEM) is 426.3 °C. Compared with the experimental data, the errors of the peak temperature predicted by ANN model and FEM are 1.56% and 0.93%, respectively. The comparison shows the validity of the FEM and ANN model.

We measured the chemical compositions of the three specimens by EDS, as shown in Fig. 5(a-c). The test data from the Vickers hardness tester were compared with the data of the trained ANN model, as shown in Fig. 5(d). The locations for the hardness measurements were 0 mm, D/4, and D/2 from the centerline. The errors between the experimental data and the ANN model ranged from 0.49 to 6.46%. The comparison demonstrated the validity of both the established and trained ANN models with respect to hardness.

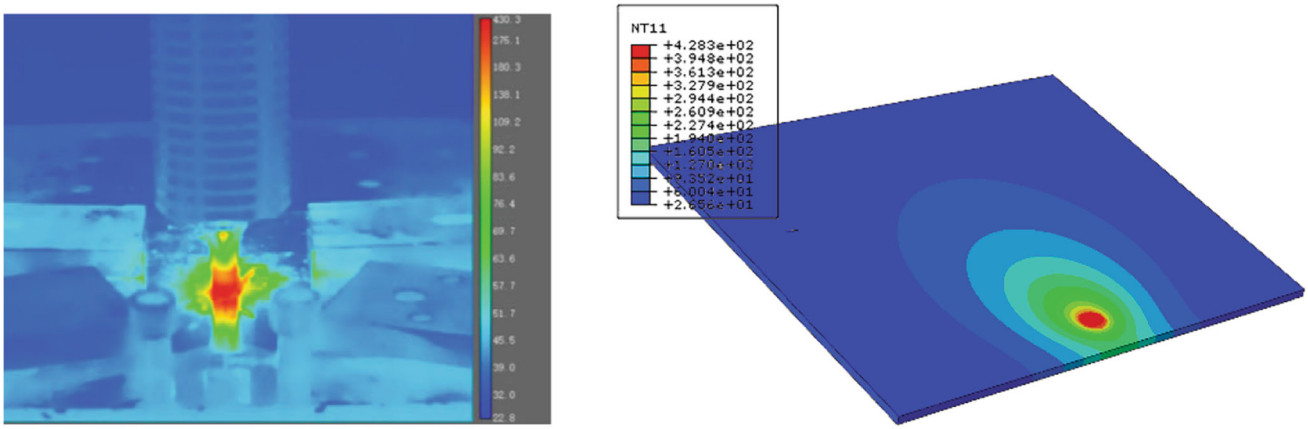

Fig. 4 Comparison of experimental and numerical temperature fields. (a) Experimental temperature field and (b) numerical temperature field

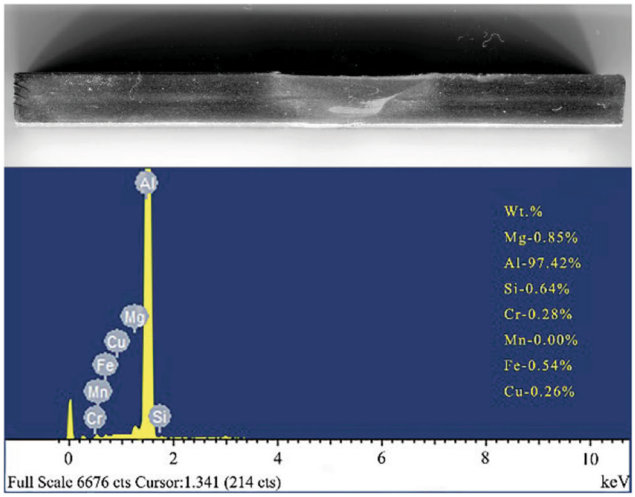

(a) Chemical compositions of specimen 1

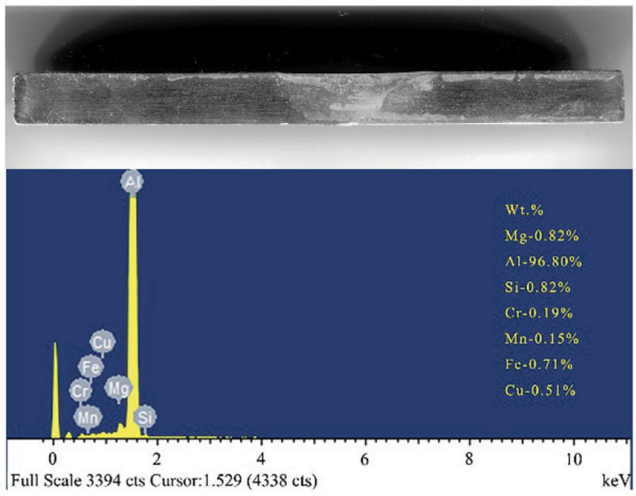

(b) Chemical compositions of specimen 2

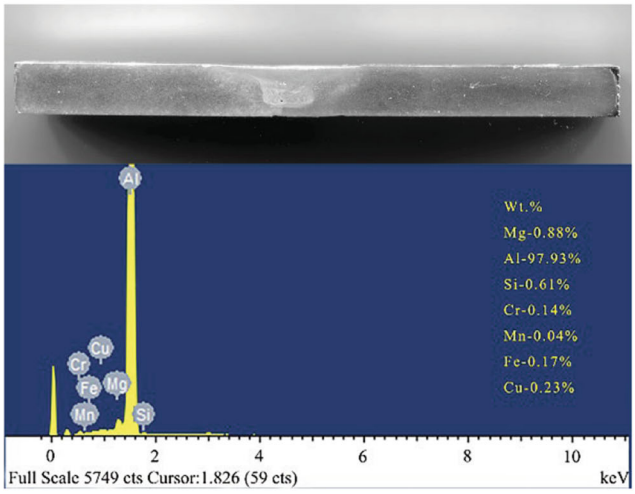

(c) Chemical compositions of specimen 3

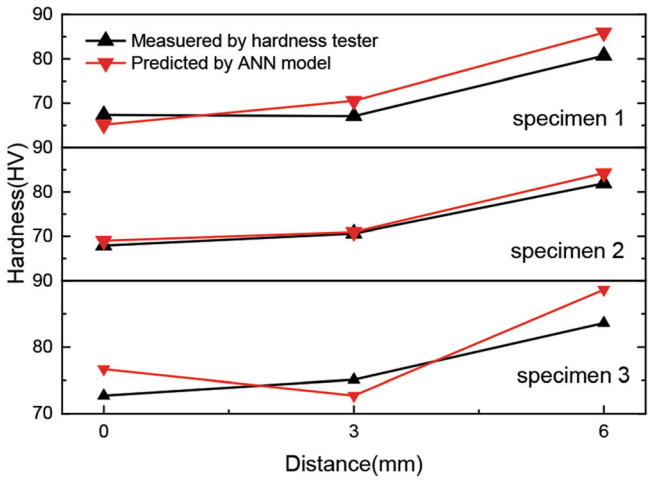

(d) Comparison of hardness between experiment and ANN model

Fig. 5 Chemical compositions measured by EDS and comparison between experimental and numerical results

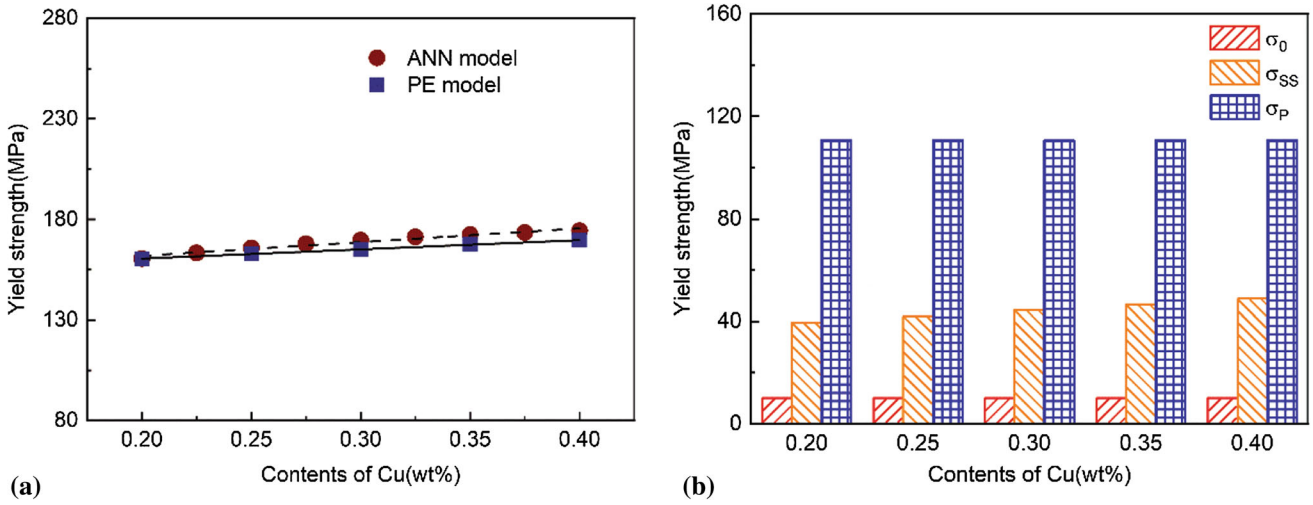

Fig. 6 Effect of Cu on mechanical properties. (a) Comparison of yield strength in different Cu contents predicted by ANN model and PEM. (b) Effect of Cu content on σ_0, σ_s and σ_p

5. Results and Discussion

The contribution of various elements in the solid solution to the yield strength (σ_{ss}) as well as the contribution of the precipitates to the yield strength (σ_p) could be calculated using the PEM. A linear relation between the hardness and yield strength was found using the following equation (Ref 26):

$$\sigma_y = 3.03\,\mathrm{HV} - 48.48. \quad \text{(Eq 20)}$$

Because of this linear relation, the yield strength could be calculated based on the predicted hardness by the data-driven model. Moreover, the yield strength could be predicted by the PEM, according to Eq 11. This allowed for the opportunity to connect data with the physical model. As indicated by Eq 11, the yield strength included contributions from pure aluminum (σ_0), precipitates, and other elements in the solid solution, among which the latter two were the main contributors to the yield strength in the 6xxx series Al alloys. The yield strength corresponded with different Cu contents in which the contents of Mg, Si, Fe, and Mn remained unchanged in the 6xxx series Al alloys, as shown in Fig. 6. The yield strength that was calculated based on the data-driven model was the same as the yield strength calculated by the PEM. The contributions of the pure aluminum and two strengthening mechanisms to the yield strength are shown in Fig. 6(b). With a 0.2 to 0.4 wt.% increase in the Cu content, σ_{SS} increased from 39.56 to 48.80 MPa, and σ_p remained unchanged. The contribution of the solid solution to the yield strength increased from 24.67 to 28.78%. On the other hand, the contribution of the precipitates to the yield strength decreased from 69.09 to 65.33%. The Cu element only existed in the solid solution and did not affect the nucleation or dissolution of the Mg_2Si. Increasing or decreasing the Cu content only affected a change in C_{Cu} of Eq 9.

The effects of the Mg and Si contents on the mechanical properties in higher Si contents are shown in Fig. 7. With a 1.0 to 1.2 wt.% increase in the Si content, σ_p remained unchanged, as shown in Fig. 7(b). The contribution of the solid solution to the yield strength increased from 21.81 to 27.06%, and the yield strength increased 7.18%. Under ideal conditions in which the relationship between the Mg and Si in the 6xxx series aluminum alloys was $C_{Mg}/C_{Si}^{eff} = 1.732$, the Mg and Si could completely react to form Mg_2Si, and no separate Mg and Si are remaining in matrix. When the Si content was higher, a part of the remaining Si existed in the solid solution after all the Mg combined with the Si to generate Mg_2Si particles. The relationship between the Mg and Si contents was $C_{Mg}/C_{Si}^{eff} < 1.732$. This was the reason that σ_p remained unchanged when the Si content increased, as in the case of higher Si content.

Figure 7(d) shows the corresponding σ_p and σ_{ss} when the Si content remained unchanged and the Mg content was increased from 1.0 to 1.2 wt.%. With an increase in Mg, the formation of Mg_2Si led to a decrease in the Si content in the solid solution, and σ_{ss} decreased from 40.32 to 29.31 MPa. Throughout this process, the nucleation rate was frequently affected by the temperature and mean solute content in the solid solution, as shown in Eq 3. With an increase in Mg, the mean solute content of Mg in the solid solution increased accordingly, and the nucleation rate also increased. This typically caused further generation of precipitate Mg_2Si particles. Figure 7(e) shows the particle number distribution of the Mg_2Si particles corresponding to the different contents of Mg. The particle number distribution corresponding to the three contents was notably similar from approximately 0 nm to 5 nm. These particles prevented dislocation motion by dislocation shear. From 5 to 12.5 nm, we observed that the number of particles corresponding to the different radii increased with an increase in Mg content. Because of the large sizes of these particles, when the dislocations interacted with the particles, the dislocations followed the Orowan mechanism and produced dislocation rings around the particles. Additionally, σ_p increased from 134.54 to 154.23 MPa when larger particles were produced with an increase in Mg content.

The effects of Mg and Si on the mechanical properties in higher Mg contents are shown in Fig. 8. When the Mg content increased, σ_p remained unchanged. However, σ_{ss} increased slightly owing to the increase in Mg content in the solid solution. The contribution of the solid solution to the yield strength increased from 44.74 to 46.28%, and the yield strength increased 2.88%. When the Mg remained unchanged at 1.0 wt.% and the Si increased from 0.4 to 0.6 wt.%, σ_{ss}

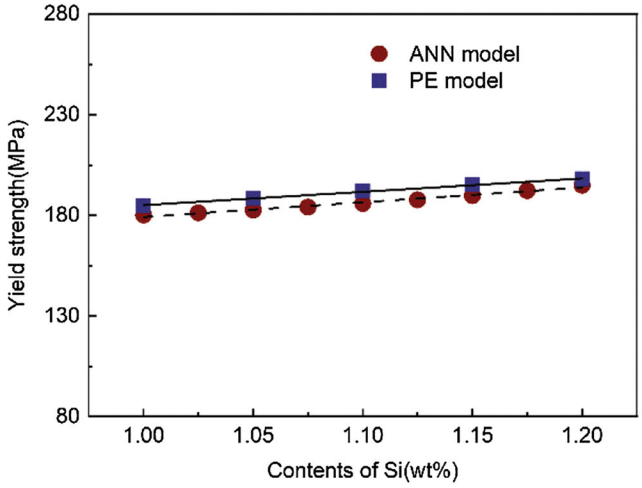

(a) Comparison of yield strength in different Si contents predicted by ANN and PEM

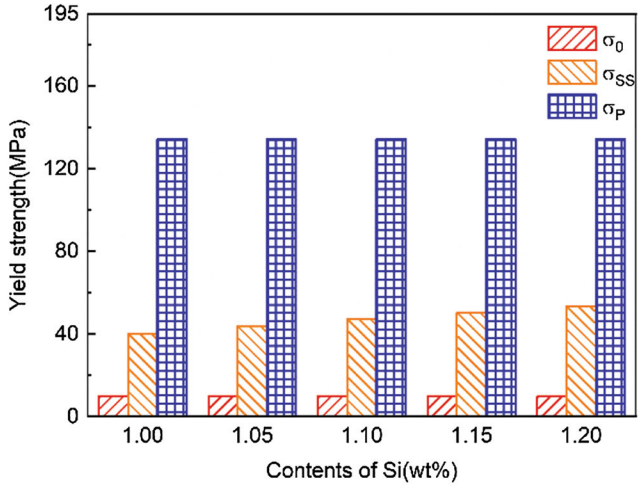

(b) Effect of Si content on σ_0, σ_s and σ_p

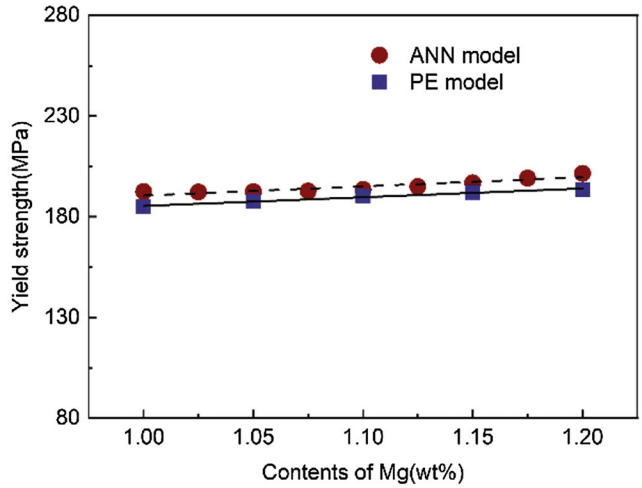

(c) Comparison of yield strength in different Mg contents predicted by ANN and PEM

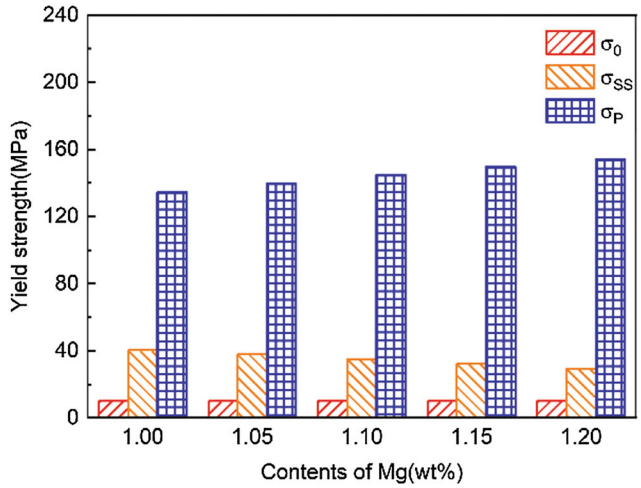

(d) Effect of Mg content on σ_0, σ_s and σ_p

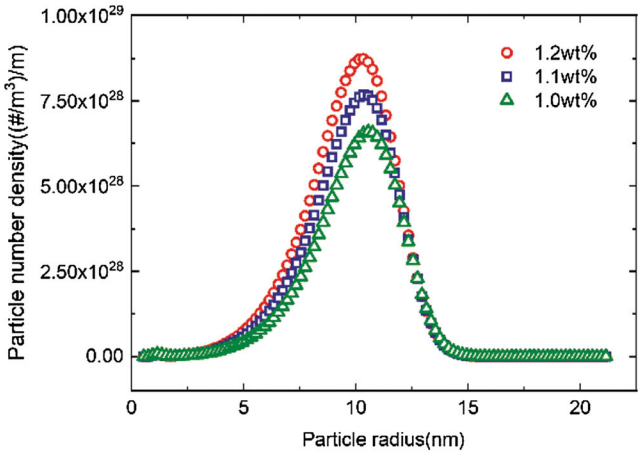

(e) Particle number density

Fig. 7 Effects of Mg and Si on mechanical properties in higher Si contents

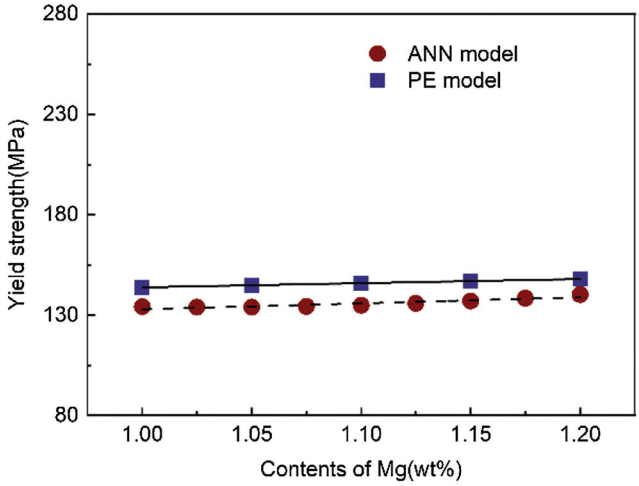

(a) Comparison of yield strength in different Mg contents predicted by ANN and PEM

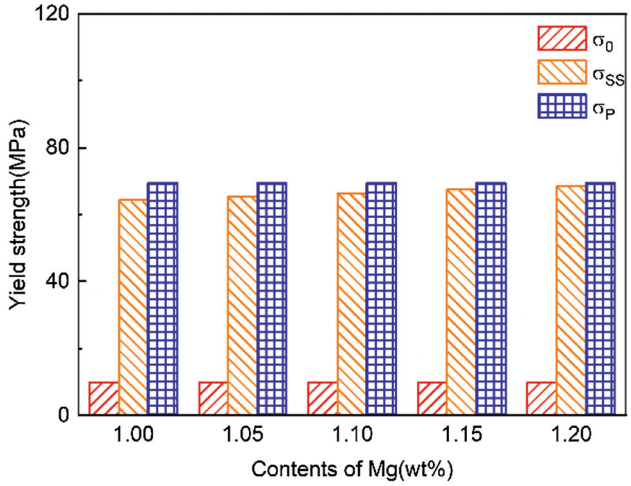

(b) Effect of Mg content on σ_0, σ_s and σ_p

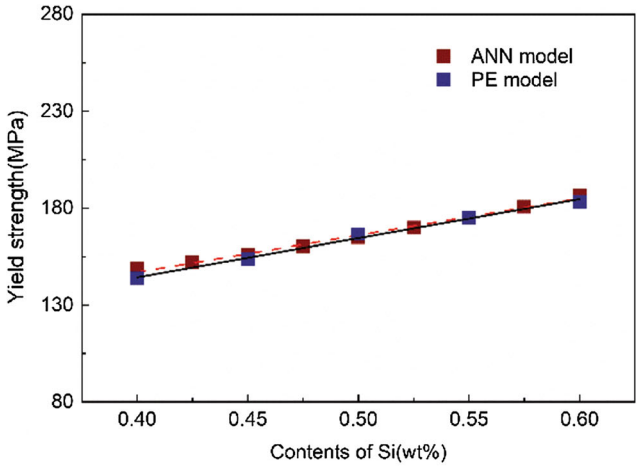

(c) Comparison of yield strength in different Si contents predicted by ANN and PEM

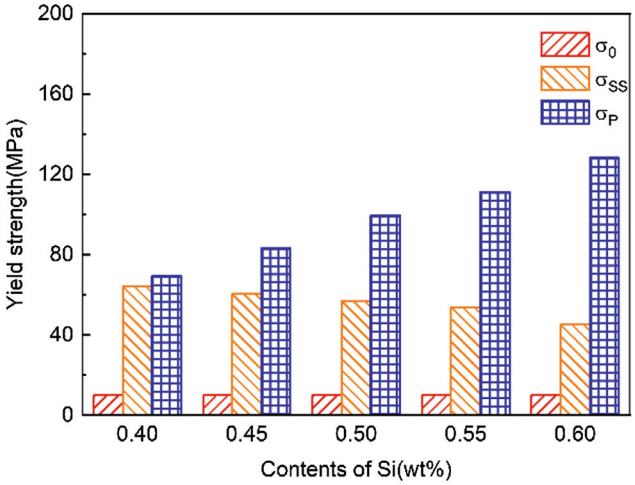

(b) Effect of Si content on σ_0, σ_s and σ_p

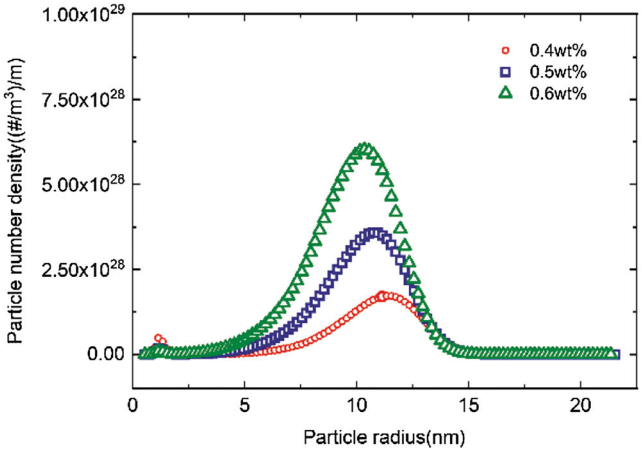

(e) Particle number density

Fig. 8 Effects of Mg and Si on mechanical properties in higher Mg contents

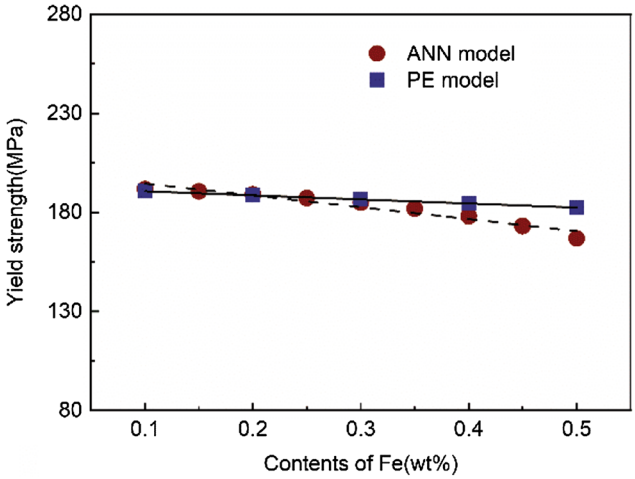

(a) Comparison of yield strength in different Fe contents in higher Si contents

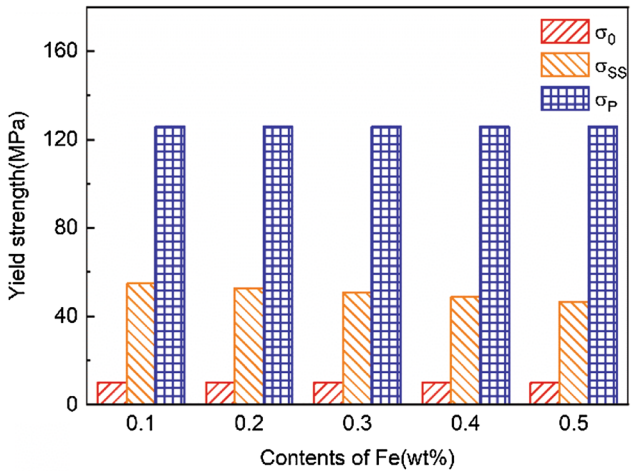

(b) Effect of Fe content on σ_0, σ_s and σ_p in higher Si contents

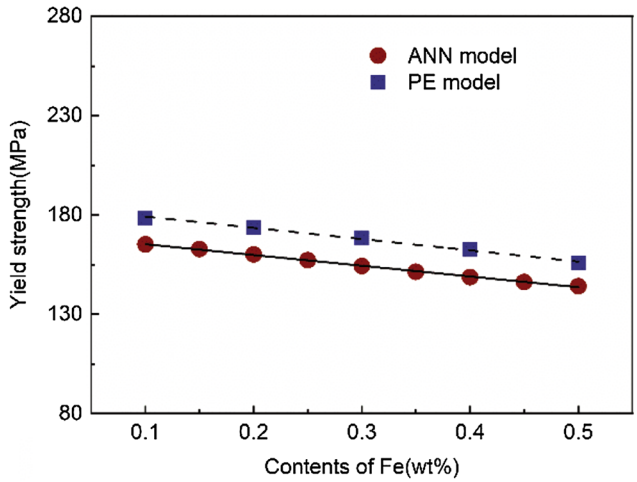

(c) Comparison of yield strength in different Fe contents in higher Mg contents

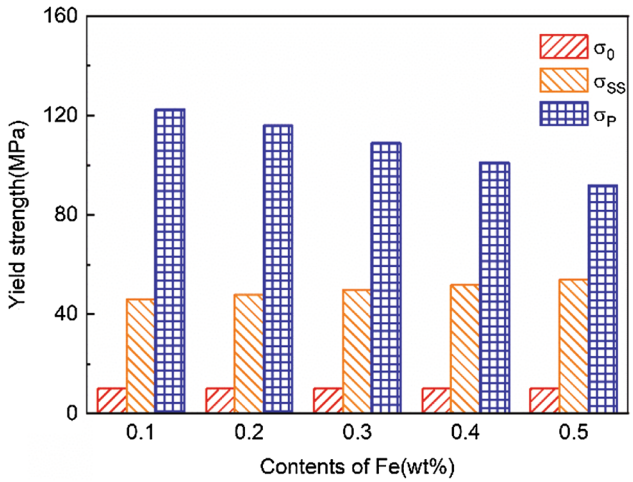

(d) Effect of Fe content on σ_0, σ_s and σ_p in higher Mg contents

Fig. 9 Effect of Fe on mechanical properties

Table 5 Summary of chemical composition effects on mechanical properties

Element	Element content, wt.%	Contribution of solid solution to yield strength, %	Contribution of precipitates to yield strength, %	Yield strength changes
Cu	0.2 → 0.4	24.67 → 28.78	69.09 → 65.32	↑ 5.76%
Si (excessive Si content)	1.0 → 1.2	21.81 → 27.06	72.78 → 67.89	↑ 7.18%
Mg (excessive Si content)	1.0 → 1.2	21.81 → 15.14	72.78 → 79.69	↑ 4.70%
Si (excessive Mg content)	0.4 → 0.6	44.74 → 24.64	48.31 → 69.91	↑ 27.56%
Mg (excessive Mg content)	1.0 → 1.2	44.74 → 46.28	48.31 → 46.95	↑ 2.88%
Fe (excessive Si content)	0.1 → 0.5	28.73 → 25.49	66.02 → 69.03	↓ 4.35%
Fe (excessive Mg content)	0.1 → 0.5	25.72 → 34.55	68.68 → 59.03	↓ 12.79%

decreased from 64.31 to 45.18 MPa and σ_p increased from 69.44 to 128.20 MPa. As the Si content increased, additional Mg_2Si particles were generated, as shown in Fig. 8(e). With an increase in Si, more precipitate particles were generated, resulting in a decrease in C_{Mg}. The contribution of the solid solution to the yield strength decreased from 44.74 to 24.64%, and the contribution of the precipitates to the yield strength increased from 48.31 to 69.90%.

When the Fe increased from 0.1 to 0.5 wt.% and the Si content was higher, the yield strength decreased slightly, as shown in Fig. 9(a). Furthermore, σ_{ss} decreased from 54.76 to 46.47 MPa, and σ_p remained unchanged, as shown in Fig. 9(b). When the Mg content was higher, σ_{ss} increased from 45.92 to 53.80 MPa and σ_p decreased from 122.63 to 91.92 MPa, as shown in Fig. 9(d). Increasing Fe promoted the generation of the intermetallic compound $Al_x(FeMn)_ySi_z$, which was observed in Ref 69. Because of the relatively larger size of this compound, it did not directly contribute to the material strengthening. However, as indicated by Eq 10, the content of effective Si in the solid solution was affected during the formation process of the compound $Al_x(FeMn)_ySi_z$. Moreover, the formation of Mg_2Si was affected because of a decrease in the effective Si content. Therefore, the Mg content in the solid solution could be increased, leading to an overall increase in the contribution of the solid solution to the yield strength.

Table 5 is a summary of the effects of chemical compositions on the mechanical properties. It was determined that the precipitates played a key role in the yield strength within a reasonable range of chemical compositions. Although an increase in Mg improved the contribution of the precipitates to the yield strength when the content of Si was higher, it also reduced the contribution of the solid solution to the yield strength. The yield strength was improved more effectively by increasing the Si. When the Mg content was higher, an increase in Si improved the yield strength by up to 27.56%. However, when the Si was higher in content, an increase in Mg only improved the yield strength by up to 4.7%.

6. Conclusion

1. In the 6xxx series Al alloys, increased Cu content improved the contribution of the solid solution to the yield strength. Meanwhile, the contribution of the precipitates to the yield strength was not affected by a change in Cu content.
2. When the Si content was higher, an increase in Si content improved the contribution of the solid solution to the yield strength. With an increase in Mg content, the contribution of the solid solution to the yield strength increased and the contribution of the hardening precipitates to the yield strength decreased.
3. When the content of Mg was higher, increasing the Si content improved the contribution of the hardening precipitates to the yield strength and the contribution of the solid solution to the yield strength decreased. The increase in Mg content improved the contribution of the solid solution to the yield strength; however, it did not affect the contribution of the hardening precipitates to the yield strength.
4. When the content of Si was higher, an increase in Fe content reduced the contribution of the solid solution to the yield strength. When the Mg content was higher, increasing the Fe content reduced the contribution of the hardening precipitates to the yield strength and increased the contribution of the solid solution to the yield strength.

Acknowledgments

This work was supported by the National Natural Science Foundation of China (No. 11572074) and Liaoning Provincial Natural Science Foundation (2019-KF-05-07).

Data Availability Statement

The raw/processed data required to reproduce these findings cannot be shared at this time because of technical or time limitations.

Conflict of interest

The authors declare that they have no conflicts of interest.

References

1. Y.Z. Li, Y.N. Zan, Q.Z. Wang, B.L. Xiao, and Z.Y. Ma, Effect of Welding Speed and Post-Weld Aging on the Microstructure and Mechanical Properties of Friction Stir Welded B4Cp/6061A1-T6 Composites, *J. Mater. Process. Technol.*, 2019, **273**, p 116242
2. F.C. Liu, P. Dong, W. Lu, and K. Sun, On Formation of Al-O-C Bonds at Aluminum/Polyamide Joint Interface, *Appl. Surf. Sci.*, 2019, **466**, p 202–209
3. S.A. Askariani, H. Pishbin, and M. Moshref-Javadi, Effect of Welding Parameters on the Microstructure and Mechanical Properties of the Friction Stir Welded Joints of a Mg-12Li-1Al Alloy, *J. Alloys Compd.*, 2017, **724**, p 859–868
4. V. Patel, W.Y. Li, A. Vairis, and V. Badheka, Recent Development in Friction Stir Processing as a Solid-State Grain Refinement Technique: Microstructural Evolution and Property Enhancement, *Crit. Rev. Solid State Mater. Sci.*, 2019, **44**, p 378–426
5. G.Q. Chen, G.Q. Wang, Q.Y. Shi, Y.H. Zhao, Y.F. Hao, and S. Zhang, Three-Dimensional Thermal-Mechanical Analysis of Retractable Pin Tool Friction Stir Welding Process, *J. Manuf. Processes*, 2019, **41**, p 1–9
6. J.L. Dong, D.T. Zhang, W.W. Zhang, W. Zhang, and C. Qiu, Microstructure and Properties of Underwater Friction Stir-Welded 7003-T4/6060-T4 Aluminum Alloys, *J. Mater. Sci.*, 2019, **54**, p 11254–11262
7. Z. Zhang and Q. Wu, Numerical Studies of Tool Diameter on Strain Rates, Temperature Rises and Grain Sizes in Friction Stir Welding, *J. Mech. Sci. Technol.*, 2015, **29**, p 4121–4128
8. S. Mironov, Y.S. Sato, and H. Kokawa, Influence of Welding Temperature on Material Flow During Friction Stir Welding of AZ31 Magnesium Alloy, *Metall. Mater. Trans. A*, 2019, **50**, p 2798–2806
9. Z. Zhang and H.W. Zhang, Numerical Studies on Controlling of Process Parameters in Friction Stir Welding, *J. Mater. Process. Technol.*, 2009, **209**, p 241–270
10. Z.Y. Wan, Z. Zhang, and X. Zhou, Finite Element Modeling of Grain Growth by Point Tracking Method in Friction Stir Welding of AA6082-T6, *Int. J. Adv. Manuf. Technol.*, 2017, **90**, p 3567–3574
11. Z. Zhang, Z.Y. Wan, L.-E. Lindgren, Z.J. Tan, and X. Zhou, The Simulation of Precipitation Evolutions and Mechanical Properties in Friction Stir Welding with Post Weld Heat Treatments, *J. Mater. Eng. Perform.*, 2017, **26**, p 5731–5740
12. J.F. dos Santos, P. Staron, T. Fischer, J.D. Robson, A. Kostka, P. Colegrove, H. Wang, J. Hilgert, L. Bergmann, L.L. Hutsch, N. Huber,

and A. Schreyer, Understanding Precipitate Evolution During Friction Stir Welding of Al-Zn-Mg-Cu Alloy Through In Situ Measurement Coupled with Simulation, *Acta Mater.*, 2018, **148**, p 163–172
13. Z. Zhang, Z.J. Tan, J.Y. Li, Y.F. Zu, W.W. Liu, and J.J. Sha, Experimental and Numerical Studies of Re-Stirring and Re-Heating Effects on Mechanical Properties in Friction Stir Additive Manufacturing, *Int. J. Adv. Manuf. Technol.*, 2019, **104**, p 767–784
14. M.A. Abdulstaar, K.J. Al-Fadhalah, and L. Wagner, Microstructural Variation Through Weld Thickness and Mechanical Properties of Peened Friction Stir Welded 6061 Aluminum Alloy Joints, *Mater. Charact.*, 2017, **126**, p 64–73
15. F. Fadaeifard, K.A. Matori, M. Toozandehjani, A.R. Daud, M.K.A.M. Ariffin, N.K. Othman, F. Gharavi, A.H. Ramzani, and F. Ostovan, Influence of Rotational Speed on Mechanical Properties of Friction Stir Lap Welded 6061-T6 Al Alloy, *Trans. Nonferrous Met. Soc. China*, 2014, **24**, p 1004–1011
16. F.C. Liu and Z.Y. Ma, Influence of Tool Dimension and Welding Parameters on Microstructure and Mechanical Properties of Friction-Stir-Welded 6061-T651 Aluminum Alloy, *Metall. Mater. Trans. A*, 2008, **39**, p 2378–2388
17. Y.S. Sato, M. Urata, and H. Kokawa, Parameters Controlling Microstructure and Hardness During Friction-Stir Welding of Precipitation-Hardenable Aluminum Alloy 6063, *Metall. Mater. Trans. A*, 2002, **33**, p 625–635
18. Z. Wang, P.W. Liu, Y.G. Xiao, X.Y. Cui, Z. Hu, and L. Chen, A Data-Driven Approach for Process Optimization of Metallic Additive Manufacturing Under Uncertainty, *J. Manuf. Sci. Eng.*, 2019, **141**, p 081004
19. Z. Wang, P.W. Liu, Y.Z. Ji, S. Mahadevan, M.F. Horstemeyer, Z. Hu, L. Chen, and L.Q. Chen, Uncertainty Quantification in Metallic Additive Manufacturing Through Physics-Informed Data-Driven Modeling, *JOM*, 2019, **71**, p 2625–2634
20. A. Majeed, J.X. Lv, and T. Peng, A Framework for Big Data Driven Process Analysis and Optimization for Additive Manufacturing, *Rapid Prototyp. J.*, 2019, **25**, p 308–321
21. W.T. Yan, S. Lin, O.L. Kafka, Y.P. Lian, C. Yu, Z.L. Liu, J.H. Yan, S. Wolff, H. Wu, E. Ndip-Agbor, M. Mozaffar, K. Ehmann, J. Cao, G.J. Wagner, and W.K. Liu, Data-Driven Multi-Scale Multi-Physics Models to Derive Process-Structure-Property Relationships for Additive Manufacturing, *Comput. Mech.*, 2018, **61**, p 521–541
22. Z. Zhang, Q. Wu, M. Grujicic, and Z.Y. Wan, Monte Carlo Simulation of Grain Growth and Welding Zones in Friction Stir Welding Of AA6082-T6, *J. Mater. Sci.*, 2016, **51**, p 1882–1895
23. Z. Zhang and C.P. Hu, 3D Monte Carlo Simulation of Grain Growth in Friction Stir Welding, *J. Mech. Sci. Technol.*, 2018, **32**, p 1287–1296
24. Z. Zhang and Z.J. Tan, A Multi Scale Strategy for Simulation of Microstructural Evolutions in Friction Stir Welding of Duplex Titanium Alloy, *High Temp. Mater. Processes (London)*, 2019, **38**, p 485–497
25. A. Simar, Y. Brechet, B. de Meester, A. Denquin, and T. Pardoen, Sequential Modeling of Local Precipitation, Strength and Strain Hardening in Friction Stir Welds of an Aluminum Alloy 6005A-T6, *Acta Mater.*, 2007, **55**, p 6133–6143
26. A. Simar, Y. Brechet, B. de Meester, A. Denquin, C. Gallais, and T. Pardoen, Integrated Modeling of Friction Stir Welding of 6xxx Series Al Alloys: Process, Microstructure and Properties, *Prog. Mater. Sci.*, 2012, **57**, p 95–183
27. H.W. Zhang, Z. Zhang, and J.T. Chen, Effect of Angular Velocity of the Pin on Material Flow During Friction Stir Welding, *Acta Metall. Sin.*, 2005, **41**, p 853–859
28. Z. Zhang and Z.Y. Wan, Predictions of Tool Forces in Friction Stir Welding of AZ91 Magnesium Alloy, *Sci. Technol. Weld. Join.*, 2012, **7**(6), p 495–500
29. Q. Wu and Z. Zhang, Precipitation-Induced Grain Growth Simulation of Friction-Stir-Welded AA6082-T6, *J. Mater. Eng. Perform.*, 2017, **26**(5), p 2179–2189
30. Z. Zhang and Q. Wu, Analytical and Numerical Studies of Fatigue Stresses in Friction Stir Welding, *Int. J. Adv. Manuf. Technol.*, 2015, **78**(9–12), p 1371–1380
31. Z. Zhang, P. Ge, and G.Z. Zhao, Numerical Studies of Post Weld Heat Treatment on Residual Stresses in Welded Impeller, *Int. J. Press. Vessels Pip.*, 2017, **153**, p 1–14
32. P. Ge, Z. Zhang, Z.J. Tan, C.P. Hu, G.Z. Zhao, and X. Guo, An Integrated Modeling of Process-Structure-Property Relationship in Laser Additive Manufacturing of Duplex Titanium Alloy, *Int. J. Therm. Sci.*, 2019, **140**, p 329–343
33. Z. Zhang, Z.J. Tan, J.Y. Li, Y.F. Zu, and J.J. Sha, Integrated Modeling of Process-Microstructure–Property Relations in Friction Stir Additive Manufacturing, *Acta Metall. Sin. (English Letters).*, 2020, **33**, p 75–87
34. M. Riahi and H. Nazari, Analysis of Transient Temperature and Residual Thermal Stresses in Friction Stir Welding of Aluminum Alloy 6061-T6 Via Numerical Simulation, *Int. J. Adv. Manuf. Technol.*, 2011, **55**, p 143–152
35. O. Frigaard, O. Grong, and O.T. Midling, A Process Model for Friction Stir Welding of Age Hardening Aluminum Alloys, *Metall. Mater. Trans. A Phys. Metall. Mater. Sci.*, 2001, **32**, p 1189–1200
36. J.H. Lienhard Iv and V.J.H. Lienhard, *A Heat Transfer Textbook*, Phlogiston Press, Massachusetts, 2003
37. M. Warmuzek, K. Rabczak, and J. Sieniawski, The Course of the Peritectic Transformation in the Al-Rich Al-Fe-Mn-Si Alloys, *J. Mater. Process. Technol.*, 2005, **162**, p 422–428
38. Y.L. Liu and S.B. Kang, The Solidification Process of Al-Mg-Si Alloys, *J. Mater. Sci.*, 1997, **32**, p 1443–1447
39. O.R. Myhr, O. Grong, and S.J. Andersen, Modelling of the Age Hardening Behaviour of Al-Mg-Si Alloys, *Acta Mater.*, 2001, **49**, p 65–75
40. S. Pogatscher, H. Antrekowitsch, and P.J. Uggowitzer, Interdependent Effect of Chemical Composition and Thermal History on Artificial Aging of AA6061, *Acta Mater.*, 2012, **60**, p 5545–5554
41. W.K. Liu, G. Karniadakis, S.Q. Tang, and J. Yvonnet, A Computational Mechanics Special Issue on: Data-Driven Modeling and Simulation-Theory, Methods, and Applications, *Comput. Mech.*, 2019, **64**, p 275–277
42. M.Z.H. Khandkar, J.A. Khan, and A.P. Reynolds, Prediction of Temperature Distribution and Thermal History During Friction Stir Welding: Input Torque Based Model, *Sci. Technol. Weld. Join.*, 2003, **8**, p 165–174
43. C.M. Chen and R. Kovacevic, Finite Element Modeling of Friction Stir Welding—Thermal and Thermomechanical Analysis, *Int. J. Mach. Tools Manuf.*, 2003, **43**, p 1319–1326
44. W. Tang, X. Guo, J.C. Mcclure, and L.E. Murr, Heat Input and Temperature Distribution in Friction Stir Welding, *J. Mater. Process. Manuf. Sci.*, 1998, **7**, p 163–172
45. S.H. Duan, Numerical Simulation of the Temperature Filed of Friction Stir Welding for 6005A-T6 Aluminum Alloy, *Electr. Weld. Mach.*, 2015, **45**, p 154–158
46. Li B (2008) Process and Mechanism of Friction Stir Welding on 6063Aluminum Alloy Sheet. Ph.D. Dissertation, Northeastern University
47. X.X. Zhang, B.L. Xiao, and Z.Y. Ma, A Transient Thermal Model for Friction Stir Weld. Part II: Effects of Weld Conditions, *Metall. Mater. Trans. A Phys. Metall. Mater. Sci.*, 2011, **42A**, p 3229–3239
48. P.C. Zhao, Y.F. Shen, G.Q. Huang, and Q.X. Zheng, Numerical Simulation of Friction Stir Butt-Welding of 6061 Aluminum Alloy, *Trans. Nonferrous Met. Soc. China*, 2018, **28**, p 1216–1225
49. J.Q. Zhang, Y.F. Shen, B. Li, H.S. Xu, X. Yao, B.B. Kuang, and J.C. Gao, Numerical Simulation and Experimental Investigation on Friction Stir Welding of 6061-T6 Aluminum Alloy, *Mater. Des.*, 2014, **60**, p 94–101
50. Z. Chi, Y.L. Liu, C.J. Li, and X.H. Yang, Effects of FSW Parameters on Residual Stress and Deformation of 6082-T6 Aluminum Alloy, *Hot Work. Technol.*, 2018, **47**, p 159–163
51. D.F. Song, W.J. Qi, T. Liang, H.Y. Wang, and N. Zhou, Influences of Post-Weld Aging Treatment on Friction Stir Welded Joints of AA6061-T6 Aluminum Alloy, *Chin. J. Rare Met.*, 2012, **36**, p 535–540
52. Y.D. Zhao, Y.Z. Zhang, and Q. He, Microstructures and Properties of Friction Stir Welding Joint of 6061-T6 Aluminum Alloy, *Mater. Mech. Eng.*, 2014, **38**, p 93–96
53. H.F. Yuan, F. Yang, Chen Liang, D.H. Shi, and M. He, Effects of Postweld Heat Treatment on Mechanical Properties of 6061 Aluminum Alloy FSW Joint, *Hot Work. Technol.*, 2018, **47**(59–62), p 70
54. T. Wang, Y. Zuo, X.M. Liu, and K. Matsuda, Special Grain Boundaries in the Nugget Zone of Friction Stir Welded AA6061-T6 Under Various Welding Parameters, *Mater. Sci. Eng. A Struct. Mater. Prop. Microstruct. Process.*, 2016, **671**, p 7–16

55. H.K. Jae, S.J. Deok, and M.K. Byung, Hardness Prediction of Weldment in Friction Stir Welding of AA6061 Based on Numerical Approach, *Procedia Eng.*, 2017, **207**, p 586–590
56. W.B. Lee, Y.M. Yeon, and S.B. Jung, Mechanical Properties Related to Microstructural Variation of 6061 Al Alloy Joints by Friction Stir Welding, *Mater. Trans.*, 2004, **45**, p 1700–1705
57. P.M.G.P. Moreira, T. Santos, S.M.O. Tavares, V. Richter- Trummer, P. Vilaca, and P.M.S.T. de Castro, Mechanical and Metallurgical Characterization of Friction Stir Welding Joints of AA6061-T6 with AA6082-T6, *Mater. Des.*, 2009, **30**, p 180–187
58. I. Shigematsu, Y.J. Kwon, K. Suzuki, T. Imai, and N. Saito, Joining of 5083 and 6061 Aluminum Alloys by Friction Stir Welding, *J. Mater. Sci. Lett.*, 2003, **22**, p 353–356
59. L. Zhou, R.X. Zhang, X.Y. Hu, N. Guo, H.H. Zhao, and Y.X. Huang, Effects of Rotation Speed of Assisted Shoulder on Microstructure and Mechanical Properties of 6061-T6 Aluminum Alloy by Dual-Rotation Friction Stir Welding, *Int. J. Adv. Manuf. Technol.*, 2018, **100**, p 1–10
60. H.T. Hsieh and J.L. Chen, Influence of Welding Parameters on Mechanical Properties of Friction Stir Welded 6061-T6 Launch Box, *Mater. Trans.*, 2008, **49**, p 2179–2184
61. Y. Uematsu, K. Tokaji, H. Shibata, Y. Tozaki, and T. Ohmune, Fatigue Behaviour of Friction Stir Welds Without Neither Welding Flash Nor Flaw in Several Aluminium Alloys, *Int. J. Fatigue*, 2009, **31**, p 1443–1453
62. Q.L. Dai, X.Y. Wang, Z.G. Hou, X. Cao, and Q.Y. Shi, Effect of Travel Speed on the Root-Defects and Mechanical Properties of Friction Stir Welded A6082 Alloy Joint, *Trans. China Weld. Inst.*, 2015, **36**, p 27–30
63. S.H. Deng, Y.L. Deng, Z. Zhang, L.Y. Ye, S. Lin, and H. Ji, Effect of Welding Parameters on Microstructure and Mechanical Properties of 6082-T6 Aluminum Alloy FSW Joint, *J. Central South Univ. (Science and Technology)*, 2018, **49**, p 55–64
64. E. Cerri, P. Leo, X. Wang, and J.D. Embury, Mechanical Properties and Microstructural Evolution of Friction-Stir-Welded Thin Sheet Aluminum Alloys, *Metall. Mater. Trans. A Phys. Metall. Mater. Sci.*, 2011, **42A**, p 1283–1295
65. M. Ericsson and R. Sandstrom, Influence of Welding Speed on the Fatigue of Friction Stir Welds, and Comparison with MIG and TIG, *Int. J. Fatigue*, 2003, **25**, p 1379–1387
66. J.D. Costa, J.A.M. Ferreira, and L.P. Borrego, Influence of Spectrum Loading on Fatigue Resistance of AA6082 Friction Stir Welds, *Int. J. Struct. Integr.*, 2011, **2**, p 122–134
67. S.Y. Kondrat'ev, Y.N. Morozova YN, Y.A. Golubev, C. Hantelmann, A.A. Naumov, and V.G. Mikhailov, Microstructure and Mechanical Properties of Welds of Al-Mg-Si Alloys After Different Modes of Impulse Friction Stir Welding, *Met. Sci. Heat Treat.*, 2018, **59**, p 697–702
68. S.Y. Ivanov, O.V. Panchenko, and V.G. Mikhailov, Comparative Analysis of Non-Uniformity of Mechanical Properties of Welded Joints of Al-Mg-Si Alloys During Friction Stir Welding and Laser Welding, *Met. Sci. Heat Treat.*, 2018, **60**, p 393–398
69. P. Donnadieu, G. Lapasset, and T.H. Sanders, Manganese-Induced Ordering in the α-(Al-Mn-Fe-Si) Approximant Phase, *Philos. Mag. Lett.*, 1994, **70**, p 319–326